Design and analysis of a PRRRP parallel mechanism for canopy vibration harvesting based on epitrochoid trajectory

Jun Pan[1], Yuechan Li[2], Puxiang Ma[2], Xinjia Cui[2], Xintao Han[2], Chanda Mulongoti[2], Hao Gao[2], Hongli Chen[2], Liang Sun[2,3], Zenghong Ma[1,2,3], Xiaoqiang Du[1,2,3*]

(1. *College of Optical, Mechanical and Electrical Engineering, Zhejiang A & F University, Hangzhou 311300, China*;
2. *School of Mechanical Engineering, Zhejiang Sci-Tech University, Hangzhou 310018, China*;
3. *Zhejiang Key Laboratory of Intelligent Sensing and Robotics for Agriculture, Hangzhou 310018, China*)

Abstract: To address the persistent challenges of low harvesting efficiency and seasonal labor shortages in *Camellia oleifera* production, this study proposes a novel canopy vibration harvester driven by a five-bar PRRRP parallel mechanism configured to generate an epitrochoid excitation trajectory. Through analysis of the epitrochoid excitation trajectory and in accordance with parallel mechanism design principles, the PRRRP configuration was selected, considering structural layout, transmission system, motion performance, and singularity distribution. On this basis, a vibration harvesting device driven by the PRRRP mechanism was designed and developed. Kinematic and dynamic analyses, as well as workspace modeling, were conducted, and real-time position acquisition of the driving components was achieved through inverse kinematics solutions. The harvesting device includes dual servo motor-driven linear modules, articulated linkages, and an adjustable excitation frame fitted with excitation rods to engage the tree canopy. Using *Camellia oleifera* cultivar of Changlin No. 40 as the target crop, the device generated an epitrochoid trajectory with a vibration frequency of 7 Hz and an amplitude of 90 mm, delivering multidirectional excitation to the canopy. By adjusting tree size parameters, the vibration response of branches with different inclination angles was investigated. The results showed that average vibration response accelerations for branches inclined at 0°-30°, 30°-60°, and 60°-90° were 14.04 m/s^2, 21.88 m/s^2, and 21.27 m/s^2, respectively, providing a theoretical basis for branch pruning. Harvesting trials indicated an overall fruit removal rate of 75.10% and an overall bud shedding rate of 11.55%, showing higher fruit removal and lower bud shedding than a traditional canopy vibration device employing linear reciprocating excitation. These results confirm that epitrochoid-based, parallel-mechanism excitation markedly improves fruit detachment efficiency and reduces collateral damage to tree architecture. Our study provides both theoretical insights and practical guidance for the development of next generation mechanized harvesters for *Camellia oleifera* and other woody fruit crops.
Keywords: canopy vibration harvesting, epitrochoid trajectory, parallel mechanism, *Camellia oleifera*
DOI: 10.25165/j.ijabe.20261903.10206

Citation: Pan J, Li Y C, Ma P X, Cui X J, Han X T, Mulongoti C, et al. Design and analysis of a PRRRP parallel mechanism for canopy vibration harvesting based on epitrochoid trajectory. Int J Agric & Biol Eng, 2026; 19(3): 159–171.

1 Introduction

In recent years, the global planting area and production of tree fruits have increased steadily. *Camellia oleifera* is one of the world's four major woody oil crops. China, as its country of origin and largest producer, had established 133 300 hm^2 of new plantations and renovated 266 700 hm^2 of existing oil-tea camellia forests by 2022, with annual tea oil production exceeding one million tons[1]. Alongside the rapid development of the tree fruit industry, global challenges such as insufficient mechanization of fruit harvesting and labor shortages have become increasingly prominent, posing serious constraints to sustainable industry growth.

To address these issues, researchers worldwide have developed various types of vibration harvesting equipment for tree fruits. Based on differences in vibration methods, this equipment can be classified into four categories: pneumatic vibration[2,3], canopy excitation[4,5], trunk excitation[6], and main branch excitation[7]. Among these methods, canopy vibration is particularly suitable for *Camellia oleifera*, which is a shrub species lacking a distinct trunk. Compared with trunk and main branch vibration harvesters, canopy vibration harvesters apply excitation forces through multi-dimensional vibration trajectories, which allow more uniform distribution of dynamic forces and reduced structural damage to trees.

Previous studies have reported notable progress in canopy and branch vibration devices. Dang et al.[8] developed a trunk-vibrating harvester for olive trees, where the vibration is applied directly to the tree trunk. The system achieved a high harvest efficiency of

Received date: 2025-09-15 **Accepted date:** 2026-05-08
Biographies: Jun Pan, PhD, Lecturer, research interest: mechanical and electrical system, Email: jpan@zafu.edu.cn; **Yuechan Li**, PhD candidate, research interest: parallel mechanisms, Email: 941016828@qq.com; **Puxiang Ma**, MS candidate, research interest: innovative design of agricultural machinery, Email: 1831317205@qq.com; **Xinjia Cui**, PhD candidate, research interest: parallel mechanisms, Email: 15003915424@163.com; **Xintao Han**, MS, research interest: innovative design of agricultural machinery, Email: 992636158@qq.com; **Chanda Mulongoti**, MS candidate, research interest: innovative design of agricultural machinery, Email: mulongotichand@gmail.com; **Hao Gao**, MS candidate, research interest: innovative design of agricultural machinery, Email: 402231431@qq.com; **Hongli Chen**, PhD, Associate Professor, research interest: mechanical and electrical system, Email: chenhldr@zstu.edu.cn; **Liang Sun**, PhD, Professor, research interest: type and dimension synthesis of mechanism, Email: liangsun@zstu.edu.cn; **Zenghong Ma**, PhD, Professor, research interest: innovative design of agricultural machinery, Email: mzhsss@126.com.
***Corresponding author: Xiaoqiang Du**, PhD, Professor, research interest: innovative design of agricultural machinery. College of Optical, Mechanical and Electrical Engineering, Zhejiang A&F University, Hangzhou 311300, China. Tel: +86-13588209025, Email: xqiangdu@163.com.

91.22%, focusing on optimizing vibration parameters like frequency and force to improve fruit detachment while minimizing tree damage. Zhang et al.[9] developed a variable-spacing comb-brush harvesting device for *Lycium barbarum*, achieving a harvesting efficiency of 90% with a damage rate of 8.41% under the optimal combination of parameters such as spring steel length and diameter. Guo et al.[10] designed a hand-pushed low-bush blueberry harvesting machine, which, after field testing, demonstrated a harvesting capacity of 12 kg/h per unit, with a fruit damage rate of 10% and a harvesting efficiency of 86%. Du et al.[11] designed a crawler-type high-clearance *Camellia oleifera* vibrating harvester, where the striking device was actuated by a crank-rocker mechanism, achieving a *Camellia oleifera* recovery rate of 87.56% and a bud shedding rate of 25.86%. Homayouni et al.[12] designed a canopy excitation-based olive harvesting machine, and field trials revealed that combining trunk vibration with canopy excitation was more effective for olive harvesting than using either method alone. Pu et al.[13] developed a two-section canopy shaker with variable frequency, achieving up to 82.6% fruit removal efficiency and minimal tree damage, highlighting the potential of adjustable vibration systems in improving mechanical harvesting. Zhuo et al.[14] identified resonant frequencies of 17.5-22.5 Hz for jujube branches via frequency sweep experiments and optimized excitation parameters using slope scoring, achieving a vibration effectiveness score of P_z= 85.63. Sola-Guirado et al.[15] developed a prototype olive harvesting machine incorporating both a trunk vibration platform and a canopy vibration platform. Field tests demonstrated that when these two platforms operated synergistically, the acceleration transfer between the trunk and branches was amplified, increasing by 8% and 17% at low and high frequencies, respectively. When the excitation frequencies of the trunk vibration and canopy vibration were set to 21.4 Hz and 3.6 Hz, respectively, the fruit detachment efficiency exceeded 85%, with losses of less than 3 kg/100 kg of harvested yield. Compared with one-dimensional trajectories, multi-dimensional vibration trajectories stimulate the target from multiple directions simultaneously, improving fruit detachment efficiency. Additionally, multi-directional excitation distributes forces more evenly on the tree, reducing the risk of structural damage.

One-dimensional vibration trajectories are commonly used in trunk vibration harvesting mechanisms and branch harvesting mechanisms. Linear reciprocating excitation, as the most common form of one-dimensional vibration trajectory, is widely used in fruit tree vibration harvesting. Rao et al.[16] introduced a hydraulically driven oil-tea fruit harvester, featuring an adjustable-spacing picking head and a matching inverted umbrella-shaped collection device, achieving an average harvesting rate of 210 fruits per minute. Du et al.[11], aiming at the growth characteristics and harvesting requirements of dwarf and dense-planted walnuts, designed a walnut harvesting equipment with adjustable vibration amplitude. This device utilizes a crank-rocker slider mechanism that outputs linear reciprocating vibration excitation. The results indicated that the harvesting rate could reach 63.9%. Malladi et al.[17] developed a portable, handheld blueberry harvesting machine. Through fruit detachment experiments conducted on rabbiteye blueberries, the results indicated that the machine could achieve a harvesting efficiency of up to 75% with a vibration duration of 3 to 4 s. Wu et al.[18] developed a crank-slider device where the crank-slider mechanism served as the actuator, achieving a fruit removal rate of up to 95.2% with a bud damage rate of 17.2%. Although such devices exhibit relatively high harvesting efficiency, their reliance on strong linear reciprocating impacts often causes considerable structural damage to trunks and branches, highlighting a key limitation of one-dimensional excitation.

Compared to linear reciprocating excitation, epitrochoid excitation achieves a higher average acceleration value with a lower coefficient of variation, indicating better acceleration uniformity and resulting in a superior overall vibration effect on fruit trees[19]. Among the various excitation trajectories for fruit trees, the epitrochoid trajectory has been proven effective for fruit harvesting. When a moving circle with a radius of r rolls (R/r+1) along the outer edge of a fixed circle with a radius of R, the trajectory of a point P on the plane where the moving circle is located forms an external rotation wheel line. Nevertheless, due to the complex rotations and translational motions inherent in epitrochoid trajectory, conventional serial mechanisms struggle to achieve the desired motion characteristics.

In contrast, parallel mechanisms offer significant advantages over serial mechanisms, including greater overall stiffness, improved dynamic performance, and higher end-effector load capacity[20]. These advantages make parallel mechanisms an attractive candidate for generating epitrochoid trajectories in fruit harvesting systems. Therefore, this study aims to develop a novel canopy vibration harvesting device for *Camellia oleifera* by employing a PRRRP-type parallel mechanism to generate an epitrochoid excitation trajectory, thereby improving fruit detachment efficiency while minimizing collateral damage to tree structure.

2 Materials and methods

2.1 Configuration synthesis and optimization of the planar five-bar mechanism

To generate the epitrochoid excitation trajectory shown in Figure 1, the harvesting mechanism must provide two translational degrees of freedom in a planar workspace. Among planar linkage systems, the five-bar mechanism is compact, structurally stiff, and capable of accurately positioning a point within a two-dimensional workspace[21,22]. Compared with three-bar and four-bar mechanisms, the planar five-bar mechanism can realize more complex trajectories while retaining a relatively simple closed-loop structure. Therefore, a planar five-bar parallel mechanism was selected as the basic candidate architecture in this study.

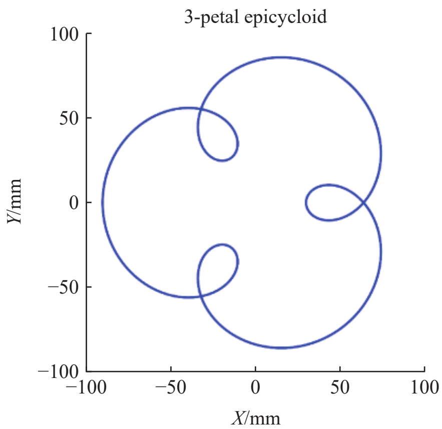

Figure 1 Epitrochoid trajectory

According to the functional requirements of canopy vibration harvesting, the candidate mechanism should satisfy the following design principles: (1) The driving components should be arranged on or near the static platform to reduce moving inertia and improve dynamic response; (2) Prismatic joints are preferred as actuated joints because they are more suitable for linear-module-based actuation; (3) Mirror configurations are counted only once, for example, PRRRR and RRRRP are regarded as the same type; and (4) One driving component should not bear the mass of another driving component. Based on these principles, six feasible planar 2-DoF five-bar configurations were retained, as shown in Figure 2.

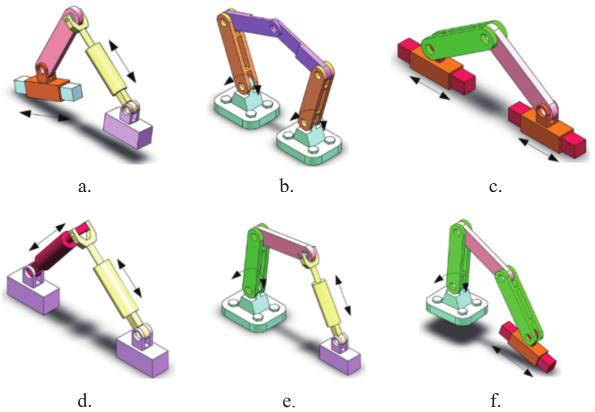

Note: Underlined text indicates the driving pair.

Figure 2 Six preferred planar 2-DoF parallel mechanisms

To strengthen the screening process, a preliminary quantitative comparison was carried out for all six candidate configurations using three countable topological indicators. The first indicator, N_b, denotes the number of actuated joints located on the fixed platform. A larger N_b is beneficial for reducing the inertia of moving parts and improving dynamic stability. The second indicator, N_p, denotes the number of prismatic actuated joints. A larger N_p is favorable for compatibility with the linear-module drive system used in this study. The third indicator, N_h, denotes the branch homology number; N_h=2 means that the left and right branches have identical joint-type sequences from the fixed platform to the end-effector, whereas N_h=0 means that the two branches are topologically different. A larger N_h is beneficial for balanced force transmission and motion consistency. Accordingly, a preliminary score S_1 was defined as

$$S_1 = 0.5\frac{N_b}{2} + 0.3\frac{N_p}{2} + 0.2\frac{N_h}{2} \tag{1}$$

where, the weight of N_b was set higher because low moving inertia is critical for continuous vibration harvesting, while N_p and N_h were used to reflect actuation compatibility and branch consistency, respectively.

The calculation results are summarized in Table 1. According to the positions of the underlined driving pairs in Figure 2, the PRRRP and RRRRR configurations show the two highest preliminary scores, reaching 1.00 and 0.70, respectively. The PRRRP configuration performs best because both actuated joints are mounted on the fixed platform, both are prismatic joints, and the two branches are topologically homologous. The RRRRR configuration ranks second because both actuated joints are also mounted on the fixed platform and the two branches are topologically homologous, although its revolute actuation is less compatible with the linear-module drive scheme. By contrast, the remaining configurations either have fewer actuators located on the fixed platform, fewer active prismatic joints, or non-homologous branch topologies. Therefore, the RRRRR and PRRRP configurations shown in Figure 2b and Figure 2c were retained as the two most promising candidate mechanisms. Their detailed kinematic characteristics were then further analyzed in the following section to determine the final configuration for the harvesting device.

Table 1 Preliminary quantitative screening of six planar 2-DoF five-bar configurations

Configuration	Active joints	N_b	N_p	N_h	S_1	Decision
PRRPR	1st P, 4th P	1	2	0	0.55	Eliminated
RRRRR	1st R, 5th R	2	0	2	0.70	Retained
PRRRP	1st P, 5th P	2	2	2	1.00	Retained
RPRPR	2nd P, 4th P	0	2	2	0.50	Eliminated
RRRPR	1st R, 4th P	1	1	0	0.40	Eliminated
RRRRP	1st R, 5th P	2	1	0	0.65	Eliminated

2.2 Kinematic analysis of the PRRRP mechanism and the 5R mechanism

2.2.1 Inverse kinematic analysis

The inverse kinematics problem for parallel mechanism, which involves determining the actuated joint values required to achieve the desired position of the moving platform (output), represents a critical aspect of the kinematic analysis of such mechanisms[23].

In this study, the PRRRP and 5R mechanisms retained from the preliminary topological screening were further analyzed as candidate mechanisms for realizing the epitrochoid excitation trajectory. Their inverse kinematics, direct kinematics, and singularity characteristics were compared to determine the final mechanism configuration.

(1) Inverse kinematic analysis of the PRRRP mechanism

The travel range of the driving components A_1 and A_2 are defined as $[0, A_{\max}]$, with the coordinates of the end-effector denoted as $P_1 = [x, y]^{\mathrm{T}}$, and the length parameters of the connecting rods defined as L and L_0. The simplified structural model of the PRRRP parallel mechanism is shown in Figure 3.

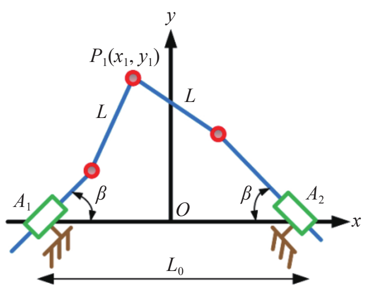

Figure 3 Schematic diagram of the PRRRP parallel mechanism

The inverse kinematics closed-loop vector equations of PRRRP mechanism are written as:

$$\begin{cases} \left(x_1 + \dfrac{L_0}{2} - A_1\cos\beta\right)^2 + (y_1 - A_1\sin\beta) = L^2 \\ \left(x_1 - \dfrac{L_0}{2} - A_2\cos\beta\right)^2 + (y_1 - A_2\sin\beta) = L^2 \end{cases} \tag{2}$$

Solving for A_1 and A_2 using kinematic inverse analysis:

$$\begin{cases} A_1 = \left(x_1 + \dfrac{L_0}{2}\right)\cos\beta + y_1\sin\beta - \sqrt{H_1} \\ A_2 = -\left(x_1 - \dfrac{L_0}{2}\right)\cos\beta + y_1\sin\beta - \sqrt{H_2} \end{cases} \tag{3}$$

where

$$H_1 = L^2 - y_1^2 - \left(x_1 + \frac{L_0}{2}\right)^2 + \left[\left(x_1 + \frac{L_0}{2}\right)\cos\beta + y_1\sin\beta\right]^2$$

$$H_2 = L^2 - y_1^2 - \left(x_1 - \frac{L_0}{2}\right)^2 + \left[\left(x_1 - \frac{L_0}{2}\right)\cos\beta - y_1 \sin\beta\right]^2$$

(2) Inverse kinematic analysis of the 5R mechanism

Figure 4 shows a 5R planar mechanism, in which C_1 and C_2 are active joints, D_1, D_2, and P_2 are passive joints, and a Cartesian coordinate system centered at the midpoint of C_1C_2, joint P_2 is considered as the reference point for the end effector.

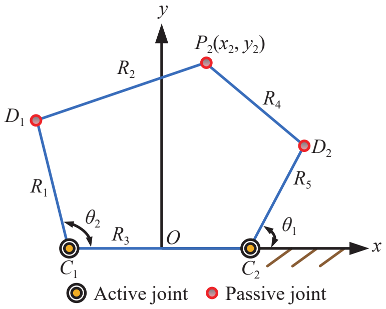

Figure 4 Schematic diagram of the 5R parallel mechanism

Set $C_1C_2 = 2R_3$, $C_1D_1 = R_1$, $D_1P_2 = R_2$, $P_2D_2 = R_4$, $C_2D_2 = R_5$. The closed-loop vector equations are derived as follows:

$$\begin{cases}(x_2 - R_3 - R_5\cos\theta_1)^2 + (y_2 - R_5\sin\theta_1)^2 = R_4^2 \\ (x_2 + R_3 - R_1\cos\theta_2)^2 + (y_2 - R_1\sin\theta_2)^2 = R_2^2\end{cases} \tag{4}$$

The joint vector θ is determined by Equation (3), providing four inverse kinematic solutions for any point within the Cartesian workspace. The expression is given below:

$$\begin{cases}\theta_1 = -\beta_1 + \arcsin F_1 \\ \theta_2 = -\beta_2 + \pi - \arcsin F_2\end{cases} \tag{5}$$

where,

$$\begin{cases}\beta_1 = \arctan\dfrac{x_2 - R_3}{y_2} \\ E_1 = \dfrac{(x_2 - R_3)^2 + y_2^2 + R_5^2 - R_4^2}{2R_5} \\ F_1 = \dfrac{E_1}{\sqrt{(x_2 - R_3)^2 + y_2^2}}\end{cases}$$

$$\begin{cases}\beta_2 = \arctan\dfrac{x_2 + R_3}{y_2} \\ E_2 = \dfrac{(x_2 + R_3)^2 + y_2^2 + R_1^2 - R_2^2}{2R_1} \\ F_2 = \dfrac{E_2}{\sqrt{(x_2 + R_3)^2 + y_2^2}}\end{cases}$$

In order to balance the moving load during the operation of the mechanism, meet the application requirements, and reduce the risk of mechanical failure, the PRRRP and 5R mechanisms have been appropriately simplified. As illustrated in Figure 5a, a Cartesian coordinate system is established to align the two moving axes of the PRRRP mechanism, with A_1A_2 located on the x-axis.

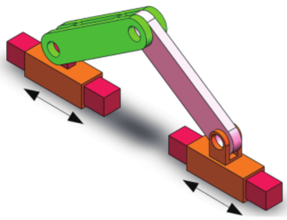

a. 3D model of the planar PRRRP parallel mechanism

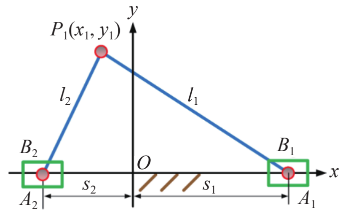

b. Schematic diagram of the planar PRRRP parallel mechanism

Figure 5 The planar PRRRP parallel mechanism

(1) PRRRP mechanism

As shown in Figure 5b, the coordinates of the end effector P_1 are denoted as (x_1, y_1). Then

$$\begin{cases}(x_1 - S_1)^2 + y_1^2 = l_1^2 \\ (x_1 - S_2)^2 + y_1^2 = l_2^2\end{cases} \tag{6}$$

where, S_1 is the distance of A_1 from the origin; S_2 is the distance of A_2 from the origin; l_1 is the length of P_1B_1; l_2 is the length of P_2B_2.

The positions of A_1 and A_2 are obtained.

$$S_i = x_1 \pm \sqrt{l_i^2 - y_1^2},\ \ i = 1,2 \tag{7}$$

According to Equation (7), the planar 2-DoF PRRRP parallel mechanism exhibits four sets of inverse kinematic solutions, each corresponding to a distinct motion mode, as shown in Figure 6.

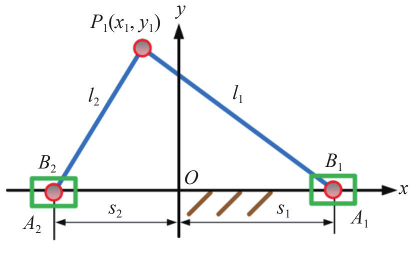

a. S_1>0, S_2<0

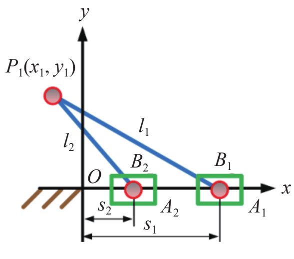

b. S_1>0, S_2>0

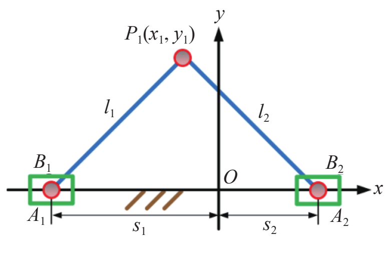

c. S_1<0, S_2>0

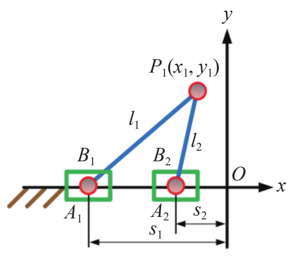

d. S_1<0, S_2<0

Figure 6 Four forms of inverse kinematic solutions of the PRRRP mechanism

(2) 5R mechanism

As shown in Figure 7b, the linkages of the 5R mechanism are of equal length and symmetrically arranged. Given the symmetrical structure, C_1C_2 coincides with the x-axis, $OC_1 = OC_2 = C_1D_1 = C_2D_2 = D_1P_2 = D_2P_2$.

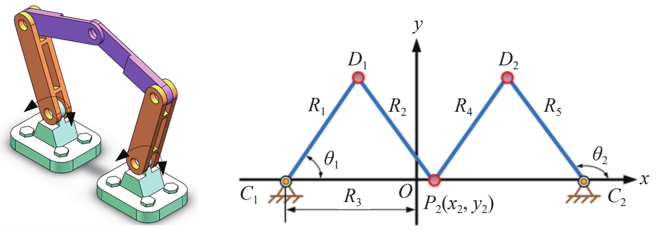

a. 3D model of the planar 5R parallel mechanism

b. Schematic diagram of the planar 5R parallel mechanism

Figure 7 The planar 5R parallel mechanism

θ_1 and θ_2 are the input angles of the C_1D_1 rod and C_2D_2 rods. The inverse solution of the position of the planar 5R parallel mechanism is solved:

$$|P_2D_i| = R_2, \quad i = 1,2 \tag{8}$$

Expanding Equation (8):

$$\begin{cases}(x_2 - R_1\cos\theta_1 + R_3)^2 + (y_2 - R_1\sin\theta_1)^2 = R_2^2\\(x_2 - R_1\cos\theta_2 - R_3)^2 + (y_2 - R_1\sin\theta_2)^2 = R_2^2\end{cases} \tag{9}$$

Given the position of the trajectory output point P_2, the input angles of the two driving rods can be obtained by Equation (10):

$$a_i\psi_i^2 + b_i\psi_i + c_i = 0 \tag{10}$$

where

$$\begin{cases}\theta_i = 2\tan^{-1}\psi_i\\ \psi_i = \dfrac{-b_i \pm \sqrt{b_i^2 - 4a_ic_i}}{2a_i}, \ (i = 1,2)\end{cases}$$

$$a_1 = R_1^2 + y_2^2 + (x_2 + R_3)^2 - R_2^2 + 2(x_2 + R_3)R_1$$

$$b_1 = -4y_2R_1$$

$$c_1 = R_1^2 + y_2^2 + (x_2 + R_3)^2 - R_2^2 - 2(x_2 + R_3)R_1$$

$$a_2 = R_1^2 + y_2^2 + (x_2 - R_3)^2 - R_2^2 + 2(x_2 - R_3)R_1$$

$$b_2 = -4y_2R_1$$

$$c_2 = R_1^2 + y_2^2 + (x_2 - R_3)^2 - R_2^2 - 2(x_2 - R_3)R_1$$

The solution of Equation (10) indicates the existence of four sets of kinematic inverse solutions, which correspond to four distinct motion modes of the 5R mechanism, as shown in Figure 8.

2.2.2 Direct kinematic analysis

The direct kinematics problem involves determining the position of the end-effector (output) of a mechanism when a set of input quantities is specified[24].

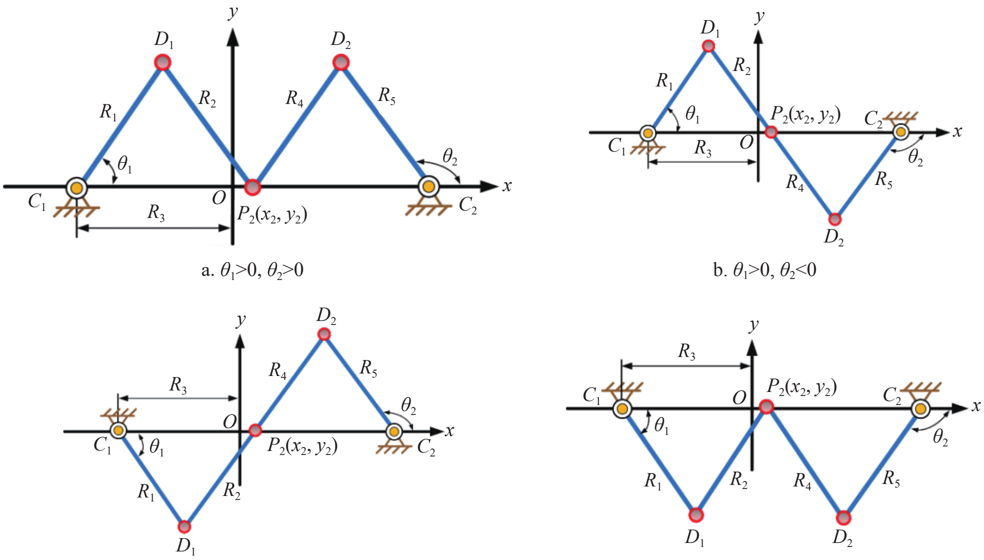

a. θ_1>0, θ_2>0

b. θ_1>0, θ_2<0

c. θ_1<0, θ_2>0

d. θ_1<0, θ_2<0

Figure 8 Four forms of inverse kinematics solutions for 5R mechanism

(1) PRRRP mechanism

The direct kinematic analysis determines the end-effector position of the mechanism for a given set of input variables, which can be obtained from Equation (6):

$$\begin{cases}S_1^2 - 2x_1S_1 + x_1^2 + y_1^2 - l_1^2 = 0\\S_2^2 - 2x_1S_2 + x_1^2 + y_1^2 - l_2^2 = 0\end{cases} \tag{11}$$

By Equation (11), it can be obtained:

$$\begin{cases}x_1 = \dfrac{S_1^2 - S_2^2 + l_2^2 - l_1^2}{2(S_1 - S_2)}\\ y_1 = \pm\sqrt{l_1^2 - (x_1 - S_1)^2}\end{cases} \tag{12}$$

Equation (12) reveals two sets of positive kinematic solutions for the PRRRP parallel mechanism: one corresponding to the 'upper form' and the other to the 'lower form' of the type of assembly. Specifically, the upper form is achieved when '+' is selected in Equation (12), whereas the lower form results when '–' is chosen, as illustrated in Figure 9.

(2) RRRRR mechanism

It can be obtained from Equation (8):

$$\begin{cases}x_2^2 + y_2^2 - 2(R_1\cos\theta_1 - R_3)x_2 - 2R_1\sin\theta_1 y_2 - 2R_1R_3\cos\theta_1 + \\ \quad R_3^2 - R_1^2 + R_2^2\\ x_2^2 + y_2^2 - 2(R_1\cos\theta_2 - R_3)x_2 - 2R_1\sin\theta_2 y_2 - 2R_1R_3\cos\theta_2 + \\ \quad R_3^2 - R_1^2 + R_2^2\end{cases} \tag{13}$$

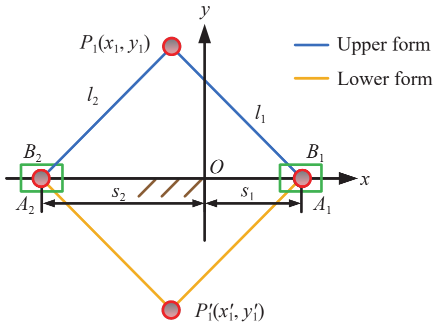

Figure 9 Two forms of direct kinematics solutions for PRRRP mechanism

Then:

$$\begin{cases} x_2 = e_2 y_2 + f_2 \\ y_2 = \dfrac{-g_2 \pm \sqrt{g_2^2 - 4d_2 h_2}}{2d_2} \end{cases} \tag{14}$$

where

$$e_2 = \frac{R_1(\sin\theta_1 - \sin\theta_2)}{2R_3 + R_1\cos\theta_2 - R_1\cos\theta_1}$$

$$f_2 = \frac{R_1 R_3(\cos\theta_1 + \cos\theta_2)}{2R_3 + R_1\cos\theta_2 - R_1\cos\theta_1}$$

$$d_2 = 1 + e_2^2$$

$$g_2 = 2(e_2 f_2 - e_2 R_1 \cos\theta_1 + e_2 R_3 - R_1 \sin\theta_1)$$

$$h_2 = f_2^2 - 2f_2(R_1\cos\theta_1 - R_3) - 2R_1R_3\cos\theta_1 + R_3^2 + R_1^2 - R_2^2$$

According to Equation (14), there exist two sets of direct kinematics solutions, which correspond to the two assembly configurations of the mechanism, specifically, the ‘upper’ and ‘lower’ configurations. When the ‘+’ sign in Equation (14) is selected, the upper configuration is obtained, whereas the ‘–’ sign corresponds to the lower configuration, as illustrated in Figure 10.

2.2.3 Singularity analysis

When the mechanism is in a singular position, it will lose control, so singular configurations should be avoided when designing and applying five bar mechanisms. One of the commonly used methods to analyze the kinematic performance of parallel mechanisms is the Jacobian-based method. By examining the Jacobian matrix, one can determine the singularity points of the parallel mechanism [25].

(1) PRRRP mechanism

The velocity mapping relationship of this mechanism is as follows:

$$A_1(\dot{s}_1 \dot{s}_2)^{\mathrm{T}} = B_1(\dot{x}_1 \dot{y}_1)^{\mathrm{T}} \tag{15}$$

In Equation (15), $(\dot{s}_1 \dot{s}_2)^{\mathrm{T}}$ is the input velocity vector of the moving part, and $(\dot{x}_1 \dot{y}_1)^{\mathrm{T}}$ is the output velocity vector of the trajectory output point P_1; A_1 and B_1 are respectively:

$$A_1 = \begin{bmatrix} x_1 - S_1 & 0 \\ 0 & x_1 - S_2 \end{bmatrix} \quad B_1 = \begin{bmatrix} x_1 - S_1 & y_1 \\ x_1 - S_2 & y_1 \end{bmatrix}$$

So, the Jacobian matrix of the PRRRP mechanism can be expressed as:

$$J_1 = A_1^{-1} B_1 = \begin{bmatrix} 1 & \pm\dfrac{y_1}{\sqrt{l_1^2 - y_1^2}} \\ 1 & \pm\dfrac{y_1}{\sqrt{l_2^2 - y_1^2}} \end{bmatrix} \tag{16}$$

(a) Actuation singularity

Based on the Jacobian matrix, the mechanism has two singular configurations. The actuation singularities therefore occur when the determinant of the output Jacobian matrix A_1 becomes zero. As shown in Figure 11a, when $x_1 = S_1$ or $x_1 = S_2$, it indicates that either the first link or the second link becomes aligned with the slider direction, which leads to ineffective actuation.

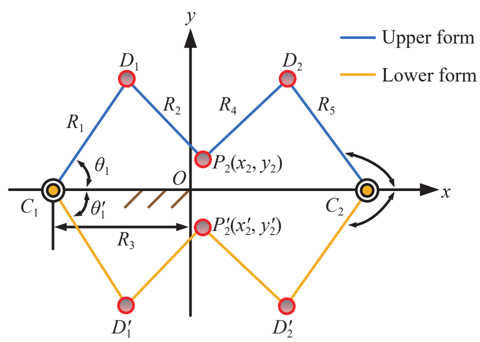

Figure 10 Two forms of direct kinematics solutions for RRRRR mechanism

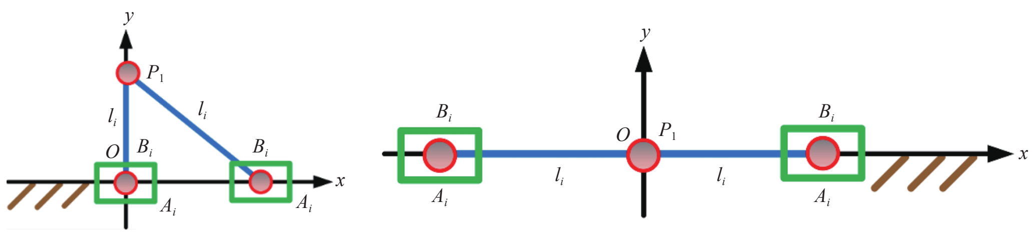

a. Singular configurations 1

b. Singular configurations 2

Figure 11 Singular configuration of the PRRRP mechanism

(b) Kinematic singularity

Kinematic singularities occur when the determinant of the output Jacobian matrix B_1 becomes zero. Thus, the kinematic singularities occur under the following conditions:

When $y_1 = 0$, meaning the moving platform point P_1 lies on the base line, causing the mechanism to collapse; When $S_1 + S_2 = 0$, implying that the two sliders are symmetrically positioned, leading to a special geometric configuration, as shown in Figure 11b.

(2) RRRRR mechanism

The velocity mapping relationship of this mechanism is as follows:

$$A_2(\dot{\theta}_1 \dot{\theta}_2)^{\mathrm{T}} = B_2(\dot{x}_2 \dot{y}_2)^{\mathrm{T}} \tag{17}$$

In Equation (17), $(\dot{\theta}_1 \dot{\theta}_2)^{\mathrm{T}}$ is the input velocity vector of the moving part, and $(\dot{x}_2 \dot{y}_2)^{\mathrm{T}}$ is the output velocity vector of the trajectory output point P_2; A_2 and B_2 are respectively:

$$A_2 = \begin{bmatrix} [y_2\cos\theta_1 - (x_2 + R_3)\sin\theta_1]R_1 & 0 \\ 0 & [y_2\cos\theta_2 + (R_3 - x_2)\sin\theta_2]R_1 \end{bmatrix}$$

$$B_2 = \begin{bmatrix} x_2 + R_3 - R_1\cos\theta_1 & y_2 - R_1\sin\theta_1 \\ x_2 - R_3 - R_1\cos\theta_2 & y_2 - R_1\sin\theta_2 \end{bmatrix}$$

So, the Jacobian matrix of the RRRRR mechanism can be expressed as:

$$J_2 = A_2^{-1}B_2 \tag{18}$$

(a) Serial singularity

According to the Jacobian matrix, when the C_1D_1 is collinear with the D_1P_2, the mechanism exhibits singularity, and the configuration of the mechanism is shown in Figure 12a and Figure 12b. When the C_2D_2 is collinear with the D_2P_2, another serial singularity occurs in the 5R mechanism, and the configuration of the mechanism is shown in Figure 12c and Figure 12d[21].

(b) Parallel singularity

When the D_1P_2 and the D_2P_2 become collinear, a parallel singularity arises. When $D_1P_2D_2$ is fully overlapped, with D_1 coinciding precisely with D_2, the corresponding singular configuration of the parallel mechanism is depicted in Figure 13(a). Here, the trajectory of P_2 traces a circle with a radius R_2 and the center of this circle is located on $\left(0, \sqrt{R_1^2 - R_3^2}\right)$ or $\left(0, -\sqrt{R_1^2 - R_3^2}\right)$, which can be determined by Equation (19). Conversely, when $D_1P_2D_2$ is fully extended, the corresponding singular configuration of the mechanism is shown in Figure 13b, and the trajectory of P_2 can be expressed by Equation (19).

$$x^2 + \left(y \pm \sqrt{R_1^2 - R_3^2}\right)^2 = R_2^2 \tag{19}$$

$$\begin{cases} x = R_1(\cos\theta_2 + \cos\theta_1)/2 \\ y = R_1\left(\sin\theta_2 + \sin\theta_1\right)/2 \end{cases} \tag{20}$$

Comparing the singularity configuration analysis results of two mechanisms, it is found that the PRRRP mechanism has fewer singular configurations, which ensures the stability of the mechanism during motion and simplifies control. Furthermore, for mechanisms requiring higher acceleration, fixing the driving joint P on the static platform results in smoother operation and a more reasonable arrangement.

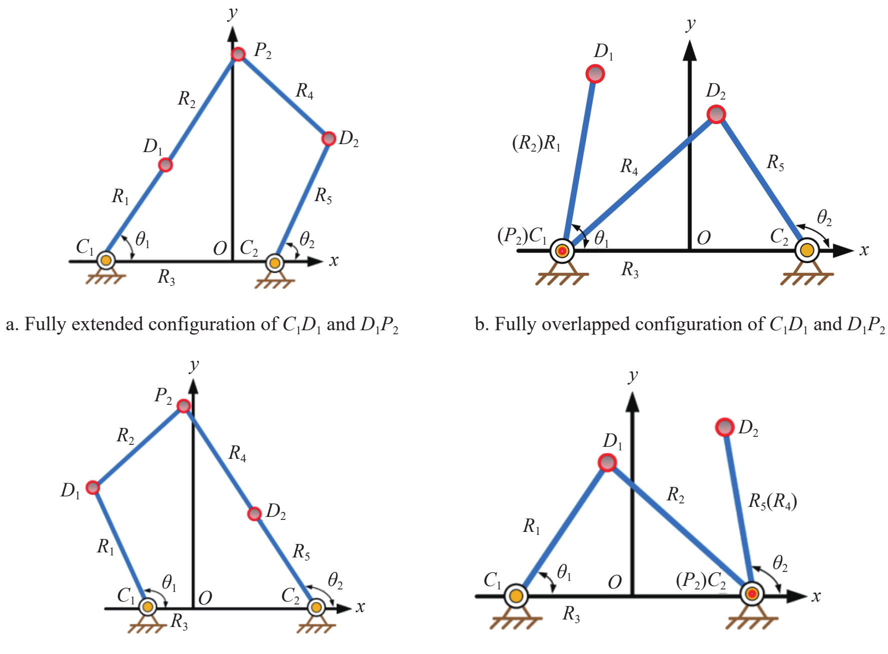

a. Fully extended configuration of C_1D_1 and D_1P_2

b. Fully overlapped configuration of C_1D_1 and D_1P_2

c. Fully extended configuration of C_2D_2 and D_2P_2

d. Fully overlapped configuration of C_2D_2 and D_2P_2

Figure 12 Serial singular physical configuration of the 5R mechanism

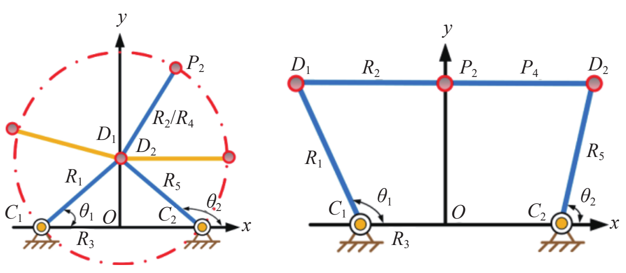

a. Fully overlapped configuration of $D_1P_2D_2$

b. Fully extended configuration of $D_1P_2D_2$

Figure 13 Singular physical shape of 5R parallel mechanism

Based on the above inverse kinematic, direct kinematic, and singularity analyses, both the PRRRP and 5R mechanisms can realize the required planar two-degree-of-freedom trajectory generation. In particular, both mechanisms exhibit four inverse kinematic solutions and two direct kinematic solutions, indicating comparable basic kinematic solvability. However, the PRRRP mechanism shows a simpler singularity distribution and fewer representative singular configurations than the 5R mechanism, which is advantageous for maintaining stable continuous excitation during canopy harvesting. In addition, the PRRRP mechanism is more compatible with the dual linear-module actuation layout adopted in this study. Therefore, after the preliminary topological screening in Section 2.1 and the detailed kinematic comparison in this section, the PRRRP parallel mechanism was finally selected as the driving mechanism of the canopy vibration harvesting device.

2.3 Workspace analysis and trajectory implementation of PRRRP parallel mechanism

2.3.1 Workspace analysis

For planar parallel mechanisms, the workspace can be defined by the position coordinates during the operation of the end effector. Therefore, the intersection of the workspaces of the two PRR serial limbs constitutes the theoretical working space of the PRRRP parallel mechanism.

When the P joint's actuation stroke is s and the length of the bar is l, the operational workspace of the PRR serial limb is shown in Figure 14, and the area of workspace is solved by Equation (21).

$$2sl+\pi l^2 \tag{21}$$

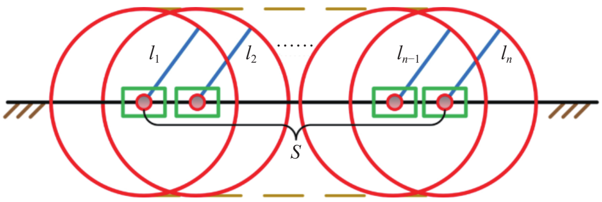

Figure 14 Theoretical workspace of PRR serial limb

2.3.2 Trajectory of excitation

The Box-Behnken experimental data obtained by the research team in the preliminary stage demonstrated that the optimal vibration effect on trees was achieved when the excitation frequency was adjusted to 7 Hz and the trajectory amplitude was set to 90 mm. Under these conditions, the trajectory of the epitrochoid can be expressed by Equation (22).

$$\begin{cases} x = 20\cos(14\pi t) - 25\cos(56\pi t) \\ y = 20\sin(14\pi t) - 25\sin(56\pi t) \end{cases} \tag{22}$$

Figure 15 shows the trajectory of the epitrochoid and the corresponding division of trajectory points under these parameter settings. In practical harvesting, singularity avoidance was implemented by restricting the target epitrochoid trajectory to the non-singular region of the PRRRP mechanism workspace. Based on the singularity analysis in Section 2.2.3, the mechanism should avoid configurations near the singular boundaries during continuous excitation. Therefore, in trajectory implementation, the workspace was not used in its entirety; instead, only the effective region that allows stable motion of the selected inverse kinematic branch was adopted for harvesting. The epitrochoid trajectory and its discrete trajectory points were arranged within this effective region, so that the mechanism could maintain continuous operation without crossing singular configurations or switching motion branches. In this way, the singularity analysis was directly incorporated into the practical trajectory planning and workspace utilization of the canopy vibration harvesting device.

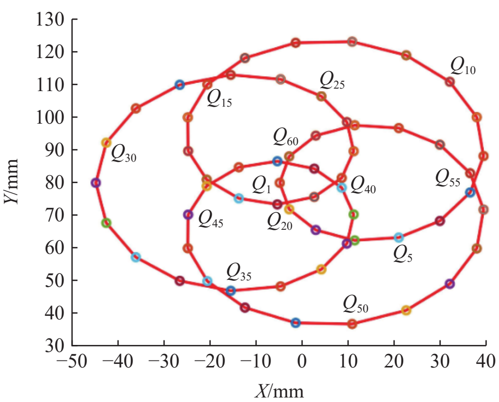

Figure 15 Epitrochoid trajectory and corresponding point segmentation

Based on the kinematic inverse solution, multiple trajectory points were generated along the epitrochoid trajectory within the preset time intervals, denoted as $Q_n (1 \le n \le 60)$. Among them, point Q_1 represents both the starting and ending point of the epitrochoid trajectory. The coordinates of these trajectory points satisfy Equation (23):

$$\begin{cases} \left(x_k - x_k^a\right)^2 + y_k^2 = l_1^2 \\ \left(x_k - x_k^b\right)^2 + y_k^2 = l_2^2 \end{cases} (k = 1,2,3\ldots n) \tag{23}$$

where, x_k^a and x_k^b are the x-axis coordinates of points A_1 and A_2 at time step k, respectively, and x_k and y_k are the x-axis and y-axis coordinates of point Q_1 at time step k.

The lengths of the first and second rods were determined according to the trajectory amplitude. To simplify processing and assembly, the two rods were designed to have equal lengths, $l_1 = l_2 = 250$ mm. The epitrochoid trajectory was equally divided into 60 segments using an interpolation method, i.e., n=60, as shown in Figure 15. The inverse kinematic equations of the PRRRP parallel mechanism were then used to calculate the initial positions of the driving components and the corresponding positions of the driving components for each trajectory point, i.e., the coordinates of points A_1 and A_2. During this process, the trajectory points were selected within the non-singular effective workspace of the mechanism, so as to ensure continuous excitation along the same motion branch in harvesting operation.

2.4 Dynamic modeling of the PRRRP mechanism

To further evaluate the dynamic characteristics of the PRRRP parallel mechanism during epitrochoid excitation, an inverse dynamic model was established using the Lagrange method. The Lagrangian of the mechanism can be expressed as

$$L = E_k - E_p \tag{24}$$

where, E_k is the total kinetic energy of the mechanism and E_p is the total potential energy. The corresponding Lagrange equation is written as

$$F_i = \frac{\mathrm{d}}{\mathrm{d}t}\left(\frac{\partial L}{\partial \dot{q}_i}\right) - \left(\frac{\partial L}{\partial q_i}\right) (i = 1,2,\ldots n) \tag{25}$$

where, q_i and $\dot{q}_i$ are the generalized coordinate and generalized velocity, respectively, and F_i is the generalized force corresponding to the i-th generalized coordinate.

The kinetic energy of each moving component of the PRRRP mechanism is composed of translational and rotational terms:

$$T_i = \frac{1}{2} m_i v_i^{\mathrm{T}} v_i + \frac{1}{2} \omega_i^{\mathrm{T}} I_i' \omega_i (i = A_1, A_2, l_1, l_2) \tag{26}$$

where, m_i, v_i, ω_i, and I_i' represent the mass, linear velocity, angular velocity, and inertia tensor of the i-th component in the global coordinate system, respectively. The total kinetic energy of the mechanism is obtained by summing the kinetic energy of the two sliders and two connecting rods. In this mechanism, the two sliders move along the zero-potential plane; therefore, only the two connecting rods contribute to the gravitational potential energy. The total potential energy can be expressed as

$$T_i = \frac{1}{2} m_i v_i^{\mathrm{T}} v_i + \frac{1}{2} \omega_i^{\mathrm{T}} I_i' \omega_i (i = A_1, A_2, l_1, l_2) \tag{27}$$

where, m_1 and m_2 are the masses of rod 1 and rod 2, respectively, and y is the vertical displacement of the trajectory output point.

For the PRRRP mechanism, inverse dynamics aims to determine the driving forces required by the two actuated sliders to realize the prescribed epitrochoid trajectory. Based on the principle of virtual work, the relationship between the generalized force vector and the actuator driving force vector can be written as

$$\tau = J^{\mathrm{T}} F \tag{28}$$

where, $\tau = (\tau_x \tau_y)^{\mathrm{T}}$ is the generalized force vector, $F = [F_1, F_2]^{\mathrm{T}}$ is the driving force vector of the two sliders, and J is the Jacobian matrix relating the slider displacements to the output motion of the end-effector. By substituting the prescribed epitrochoid trajectory, velocity, and acceleration into the dynamic model, the real-time driving forces F_1 and F_2 required by the two actuated sliders can be obtained.

2.5 Design of the PRRRP-driven canopy vibration harvesting device

According to the growth environment and characteristics of *Camellia oleifera* tree, a canopy vibration device driven by a PRRRP parallel mechanism based on the trajectory of the epitrochoid was designed, which was composed of a driving mechanism, an excitation mechanism, and a fixed frame, as shown in Figure 16. Before harvesting, the desired excitation frequency is achieved by adjusting the rotation speed of the servomotor output shaft. During operation, the excitation rods are inserted into the target canopy, the frame is kept stable, and the driving mechanism is started to output the epitrochoid trajectory.

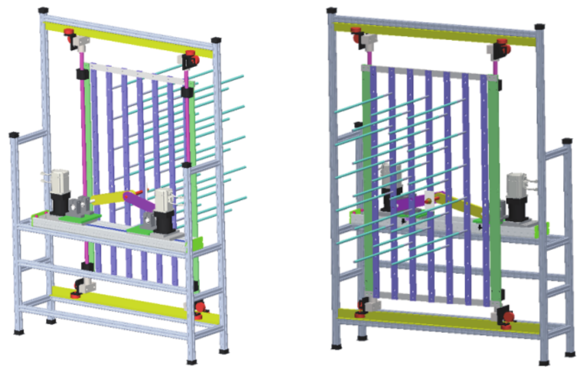

Figure 16 3D model of the harvesting device

The driving mechanism is a PRRRP parallel mechanism composed of double sliding table linear module, reducer, servo motor, rod 1, rod 2, output shaft, etc., as shown in Figure 17. The output of servo motor and reducer drives sliding table 1 and sliding table 2 to achieve linear movement, and rod 1 and rod 2 to coordinate movement, driving the output shaft to achieve different forms of movement trajectory.

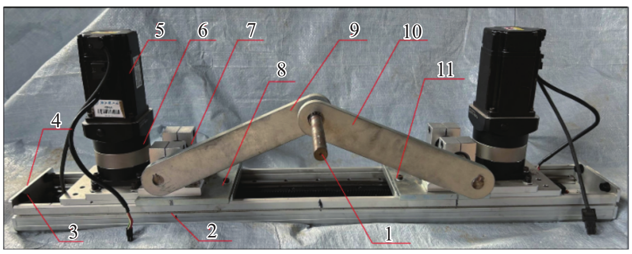

1. Output shaft 2. Linear module 3. Rubber pad 4. Limiting baffle 5. Servo motor 6. Reducer 7. Bearing seat 8. Slide table 1 9. Rod 1 10. Rod 2 11. Slide table 2

Figure 17 Driving mechanism

The excitation mechanism comprises an excitation frame, multiple excitation rods, and a sliding mechanism, as illustrated in Figure 18. The sliding mechanism facilitates synchronous vertical movement of sliders along the sliding axis and drives the translation of the guide wheel mounting plate. The excitation rods are arranged in a staggered configuration, with a horizontal spacing of 20 cm and a vertical spacing of 16 cm[26]. Each rod measures 50 cm in length (considering that oil-tea camellia fruits are predominantly concentrated in the outer 50 cm of the canopy), and they are mounted onto the frame via fixing rings[27]. The insertion depth of the rods can be adjusted according to the canopy width of the *Camellia oleifera* trees.

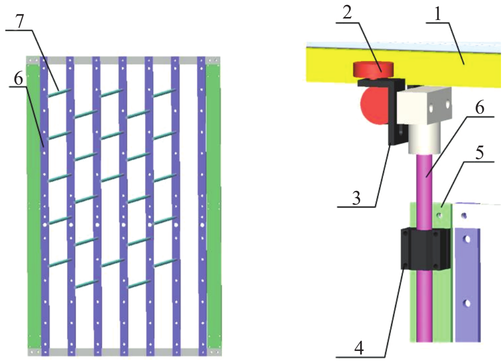

1. Guide rail 2. Guide wheel 3. Guide wheel fixing plate 4. Slider 5. Excitation frame 6. Sliding shaft 7. Excitation rod

Figure 18 3D model of the excitation mechanism

In practical canopy harvesting, the spatial adaptability of the device is considered in two directions. Along the excitation-rod axis, the rod length and adjustable insertion depth allow the excitation structure to reach the outer fruit-bearing layer of the *Camellia oleifera* canopy. Perpendicular to the rod axis, the PRRRP mechanism provides an epitrochoid trajectory with an amplitude of 90 mm, corresponding to a transverse span of about 180 mm. Combined with the staggered multi-rod excitation structure adopted in the device, the mechanism can cover the target local canopy region and meet the workspace requirement of canopy vibration harvesting.

2.6 Simulation of the canopy vibration device

To verify the kinematic performance of the canopy vibration device, a virtual prototype simulation was conducted using ADAMS. The kinematic simulation was performed with a simulation time of 1 s and 500 steps. As shown in Figure 19, the trajectory of the excitation rod perfectly matches the desired epitrochoid trajectory, and the displacement, velocity, and acceleration of the excitation rod are presented in Figure 20, Figure 21, and Figure 22, respectively.

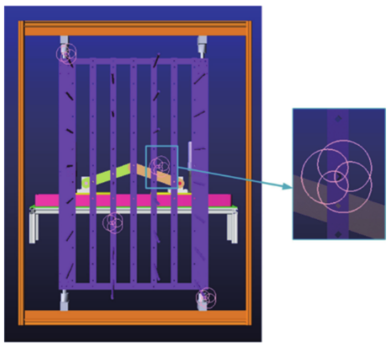

Figure 19 Motion path of excitation rod

As shown in Figures 20-22, the maximum vibration amplitudes of the excitation rod in the x and y directions were 89.85 mm, the maximum velocity reached 4.52 m/s, and the maximum acceleration was 616.81 m/s^2, which meets the operational requirements for vibration-based harvesting of fruit trees. The simulated displacement and velocity curves are smooth and periodic, which is consistent with the continuous epitrochoid motion generated by the coordinated movement of the two linear modules. The acceleration peak appears at the high-curvature segments of the trajectory and near the rapid change of motion direction, which is a normal dynamic feature of epitrochoid excitation rather than an abnormal impact of the mechanism. It should also be noted that the peak value of 616.81 m/s^2 corresponds to the excitation rod itself, whereas the vibration transmitted to the tree canopy is significantly attenuated by the rod-canopy contact and the compliance of the branch-canopy system. This is consistent with the field-test results, in which the measured canopy response accelerations were much lower and the bud shedding level remained low, indicating that the selected excitation parameters can provide effective fruit detachment without causing excessive damage to the tree body.

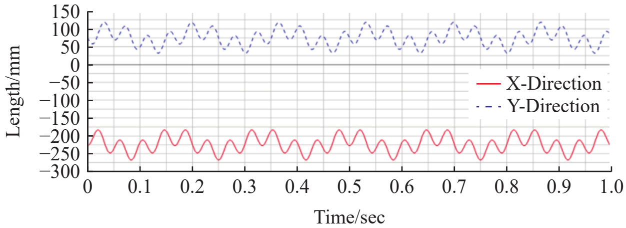

Figure 20 Displacement-time simulation results of the excitation rod

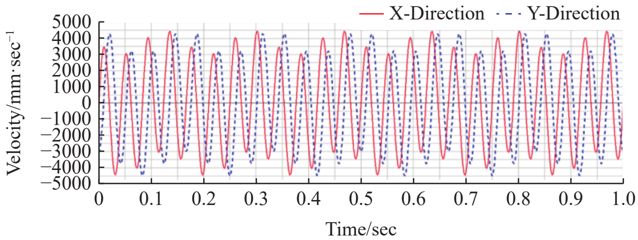

Figure 21 Velocity-time simulation results of the excitation rod

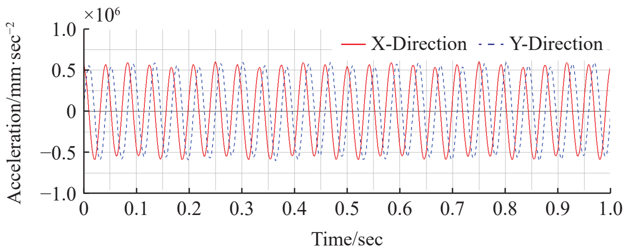

Figure 22 Acceleration-time simulation results of the excitation rod

To verify the dynamic model, a virtual prototype of the PRRRP mechanism was established in ADAMS. The 3D model created in SolidWorks was imported into ADAMS, and the material of the mechanism was set as aluminum, as shown in Figure 23. Two prismatic joints and three revolute joints were defined according to the actual kinematic constraints of the PRRRP mechanism. The displacement inputs of the two sliders, obtained from the inverse kinematic solution of the epitrochoid trajectory, were imported into ADAMS using spline functions. The simulation time was set to 1 s with 500 steps.

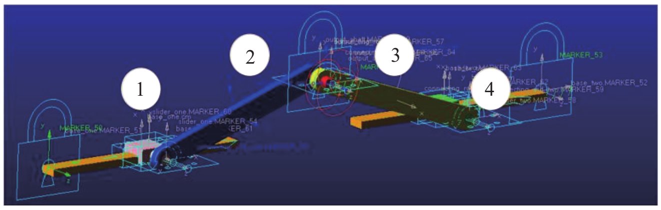

1. Slider 1 2. Rod 1 3. Rod 2 4. Slider 2

Figure 23 PRRRP parallel mechanism model established in ADAMS

The main physical parameters used in the dynamic simulation are listed in Table 2. The masses of slider 1 and slider 2 were both 0.173 kg, and the masses of rod 1 and rod 2 were both 0.801 kg. In addition, a 15-kg load was applied to the end-effector to represent the excitation structure and canopy-contact load during operation.

Table 2 Main physical parameters of the PRRRP mechanism used in dynamic simulation

Component	Mass/kg	Initial global coordinate/mm	Inertia tensor/kg·mm^2
Slider 1	0.173	(241.85,0,0)	/
Rod 1	0.801	(–123.43,40,38.5)	blkdiag (72.24,4679.53,4729.19)
Rod 2	0.801	(–123.43,40,38.5)	blkdiag(72.24,4679.53,4729.19)
Slider 2	0.173	(231.85,0,0)	/

The comparison shows that the theoretical and simulated driving force curves of the two actuated sliders are consistent in trend and exhibit smooth periodic variations during one excitation cycle. As shown in Figure 24, the maximum driving force of slider 1 was 1279.65 N, and that of slider 2 was 1236.06 N. The relative error between the theoretical calculation and ADAMS simulation was 0.22%-5.88% for slider 1 and 0.84%-7.41% for slider 2, with a maximum relative error of 7.41%, which is within an acceptable range for dynamic simulation and verifies the validity of the proposed dynamic model.

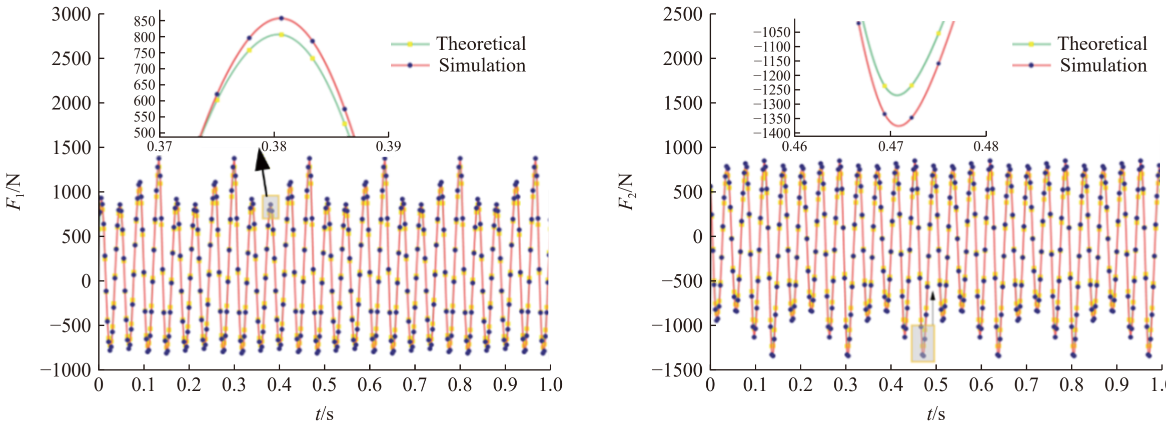

a. Driving force of slider 1 b. Driving force of slider 2

Figure 24 Comparison between theoretical calculation and ADAMS simulation results

These results indicate that the PRRRP mechanism can generate the required epitrochoid excitation trajectory with controllable actuator loads. In addition, the smooth and periodic driving-force curves suggest that no severe force mutation occurs during continuous operation, which is beneficial for maintaining stable excitation and reducing impact on the mechanism and canopy.

2.7 Control system

The canopy vibration-based harvesting machine achieves an epitrochoid trajectory through the actuation of a PRRRP parallel mechanism, necessitating synchronous control of the rotational speed and angle of two servo motors via a microcontroller. The hardware system includes a computer, microcontroller, servo drives, servo motors, and incremental photoelectric encoders. The real-time rotation angle of the motor is determined based on the real-time position information of the linear module slide table. Programming for motor control is implemented on the Keil MDK5 platform. The microcontroller outputs digital pulse signals to the servo drivers, which in turn activate the servo motors to execute tasks. Closed-loop control is achieved through incremental optical encoders, ensuring precise movement (Figure 25).

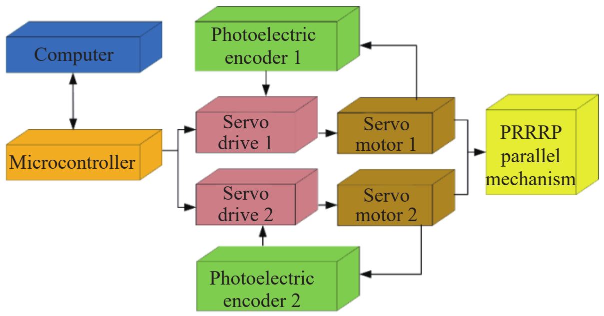

Figure 25 Control system for the drive mechanism

In actual field operation, uneven terrain may indirectly affect the stability of the output epitrochoid trajectory by causing slight inclination or vibration of the machine frame, which changes the relative pose between the excitation rods and the canopy. As a result, small deviations in rod insertion depth and contact force may occur, leading to minor fluctuations in the trajectory transmitted to the branches during continuous operation. Nevertheless, because the two actuators of the PRRRP mechanism are mounted on the static frame and synchronized through closed-loop servo control, the mechanism can still maintain stable motion in its local coordinate system. Therefore, maintaining frame stability during operation is important; for future field applications, chassis leveling, improved ground support stiffness, and real-time synchronization compensation of the two linear modules could be used to further enhance trajectory stability.

3 Results and discussion

3.1 Vibration response test of *Camellia oleifera* canopy

The tested trees were upright and compact "Changlin No. 40" *Camellia oleifera* trees with good growth and high yield, aged 13–14 years. To improve the repeatability and comparability of the field tests, the basic morphological parameters of the sampled trees were supplemented based on the measured structural characteristics of the same cultivar in the same orchard. The average trunk height was 322.5±96.6 mm, and the average trunk diameter was about 107.6 mm. The first-order branches had an average length of 2145.4±398.7 mm, basal diameter of 71.3±12.6 mm, distal diameter of 18.9±6.9 mm, average inclination angle of 16.5°±10.6°, and number of 4±2. The second-order branches had an average length of 1369.2±437.2 mm, basal diameter of 34.2±11.0 mm, distal diameter of 15.9±5.5 mm, average inclination angle of 30.5°±13.6°, and average number of 5±3.

Vibration acceleration tests were conducted on the canopy regions of *Camellia oleifera* trees where secondary or tertiary branches with different inclination angles were located. Based on the inclination angle of the secondary and tertiary branches relative to the ground, three groups were defined: horizontal branches with angles ranging from 0°-30°, inclined branches with angles ranging from 30°-60°, and vertical branches with angles ranging from 60°-90°, as shown in Figure 26. The selected branches exhibited similar morphological characteristics to the surrounding canopy.

Figure 26 Arrangement positions of acceleration sensors

Two three-axis acceleration sensors were fixed onto the target branches. Before the test, the excitation rods mounted on the vibration frame were inserted into the canopy of the target *Camellia oleifera* tree. The servo motor was then activated to drive the PRRRP parallel mechanism, generating an epitrochoid trajectory. The forced vibration acceleration of the canopy, corresponding to the branches in the three inclination groups, was recorded using the three-axis acceleration sensors. Each vibration test lasted for 5 s. The experimental schematic diagram is shown in Figure 27.

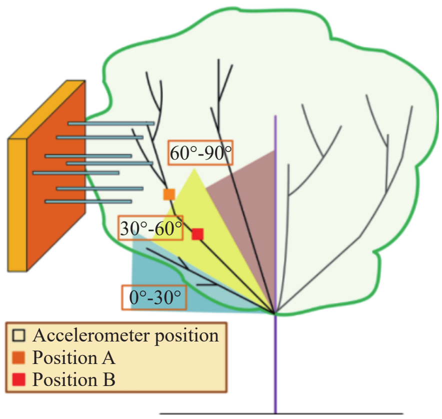

Figure 27 The experimental schematic diagram

Data acquisition was performed using a data acquisition and analysis system in combination with three-axis acceleration sensors. The average synthetic acceleration was calculated according to Equation (29). The statistical results of the canopy vibration acceleration of *Camellia oleifera* are shown in Figure 28.

$$\bar{a} = \sqrt{a_x^2 + a_y^2 + a_z^2} \tag{29}$$

where, a_x is the vibration acceleration of the branch in the x-direction, m/s²; a_y is the vibration acceleration in the y-direction, m/s²; and a_z is the vibration acceleration in the z-direction, m/s².

The average vibration response accelerations of the *Camellia* *oleifera* canopy corresponding to branch growth postures of 0°-30°, 30°-60°, and 60°-90° were 14.04 m/s², 21.88 m/s², and 21.27 m/s², respectively. A comparison of acceleration values measured by sensors placed at different positions revealed that the acceleration values increased as the sensors were positioned closer to the free end of the branches. Therefore, *Camellia oleifera* trees with smaller canopy radial dimensions, compact structures, and generally upright branches are more suitable for mechanized harvesting. These findings also provide guidance for pruning *Camellia oleifera* trees: it is recommended to retain inclined branches with growth angles of 30°-60° and vertical branches with growth angles of 60°-90°, while appropriately removing horizontal branches with angles of 0°-30° or overly thick branches.

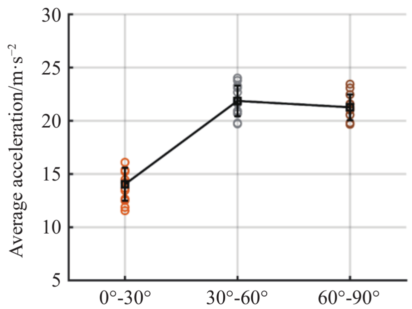

Figure 28 Vibration acceleration of the *Camellia oleifera* canopy

3.2 Harvesting experiment results and analysis

The vibration frequency was set to 7 Hz and the amplitude to 90 mm. Due to the limited contact area of the canopy excitation harvesting mechanism, it was unable to cover the entire *Camellia oleifera* tree. Therefore, individual *Camellia oleifera* canopies were selected as the test objects, with a total of six groups included in the experiment. Before harvesting, the number of fruits and flower buds within each canopy was recorded. During harvesting, the excitation rods of the mechanism were inserted into the *Camellia oleifera* canopy, and the servo motor was activated to drive the mechanism, generating an epitrochoid trajectory for 10 s. After harvesting, the number of fallen fruits and flower buds was recorded. The harvest test site is shown in Figure 29. The fruit net harvesting rate and flower bud shedding rate were calculated according to Equations (30) and (31), respectively.

$$I_1 = \frac{n_1}{n_1 + n_2} \times 100\% \tag{30}$$

$$I_2 = \frac{n_3}{n_3 + n_4} \times 100\% \tag{31}$$

where, n_1 is the number of fallen fruits; n_2 is the number of fruits left on the tree; n_3 is the number of fallen flower buds; n_4 is the number of flower buds left on the tree.

Figure 30 shows the fruit harvesting rate and bud shedding rate of the canopy excitation harvesting mechanism.

a. b. c.

Figure 29 Harvest test site

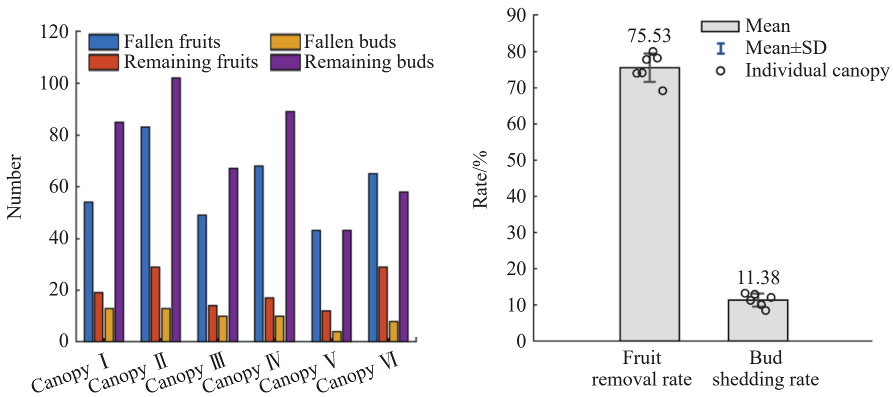

a. Count statistics of fruits and buds

b. Mean values with standard deviation

Figure 30 Statistics on fruit harvesting rate and bud shedding rate

Figure 30a shows the fallen and remaining fruits and buds for each canopy group, while Figure 30b presents the mean fruit removal rate and bud shedding rate with standard deviation error bars based on the six canopy groups. The group-wise mean fruit removal rate was 75.53%±3.93%, ranging from 69.15% to 80.00%, whereas the group-wise mean bud shedding rate was 11.38%±1.82%, ranging from 8.51% to 13.27%. When the count data from all six canopy groups were pooled, the overall fruit removal rate and bud shedding rate were 75.10% and 11.55%, respectively, which were consistent with the group-wise statistical results. The coefficient of variation of fruit removal rate was 5.20%, indicating relatively low dispersion and good consistency among the six canopy groups. By comparison, the coefficient of variation of bud shedding rate was 16.01%, showing a larger relative fluctuation, although the overall bud shedding level remained low. These results indicate that the canopy vibration harvesting device driven by the PRRRP parallel mechanism could achieve relatively stable fruit detachment while maintaining limited bud loss. Compared with the canopy vibration device driven by a crank-slider mechanism reported by Chen et al.[28], which achieved a fruit removal rate of 69.1% and a bud shedding rate of 13.13%, the present device exhibited a higher fruit removal rate and a lower bud shedding rate. These results further indicate that the epitrochoid excitation trajectory provides better harvesting performance than the conventional one-dimensional reciprocating trajectory and offers technical support for the development of canopy vibration harvesting equipment.

4 Conclusions

This study proposes a parallel canopy excitation harvesting device that enhances fruit harvesting efficiency and reduces flower bud shedding by utilizing an epitrochoid excitation trajectory. The design of the vibration excitation device emphasizes structural compactness, stability, high precision, and excellent vibration resistance. Through a comprehensive analysis of structural configurations, drive modes, layout schemes, velocity and dynamic characteristics, and singularity conditions, the PRRRP mechanism was identified as the optimal configuration. Dynamic verification showed that the maximum driving forces of slider 1 and slider 2 were 1279.65 N and 1236.06 N, respectively. Based on this, a prototype was designed and assembled, consisting of a planar PRRRP mechanism, a vibration excitation unit, and a supporting frame. The PRRRP parallel mechanism was driven by servo motors to generate the desired epitrochoid vibration trajectory. Finally, field experiments were conducted on *Camellia oleifera* cv. Changlin 40. The vibration response test results showed that the vibration response acceleration under three branch growth postures of 0°-30°, 30°-60°, and 60°-90° was 14.04 m/s^2, 21.88 m/s^2, and 21.27 m/s^2, providing guidance for branch pruning. The experiment was conducted with harvesting rate and flower bud shedding rate as key evaluation indicators. The experimental results showed that the average removal rate was 75.10%, and the flower bud shedding rate was as low as 11.55%, effectively verifying the superior performance of the parallel PRRRP-driven canopy vibration harvesting mechanism in fruit harvesting applications.

Acknowledgements

This work was supported by the National Key Research and Development Program of China (Grant No. 2022YFD2202103-4), the R&D Project of National Innovation Park for Forestry and Grass Equipment (Grant No. 2024YG06), and the Zhejiang Provincial Key Research & Development Program (Grant No. 2025C02202, 2023C02049).

[References]

[1] Chen J P, Wang Y D, Zhou H P. Research on *Camellia oleifera* fruit harvesting machinery and sorting technology. Journal of Forestry Engineering, 2024; 9(4): 12–24. (in Chinese)

[2] Whitney J, Wheaton T. Shakers affect Florida orange fruit yields and harvesting efficiency. Applied Engineering in Agriculture, 1987; 3(1): 20–24.

[3] Aragon-Rodriguez F, Castro-Garcia S, Sola-Guirado R R, Gil-Ribes J A. Fruit abscission pattern of 'Valencia' orange with canopy shaker system. Scientia Horticulturae, 2019; 246: 916–920.

[4] Castro-Garcia S, Sola-Guirado R R, Gil-Ribes J A. Vibration analysis of the fruit detachment process in late-season 'Valencia'orange with canopy shaker technology. Biosystems Engineering, 2018; 170: 130–137.

[5] Colmenero-Martinez J T, Blanco-Roldán G L, Bayano-Tejero S, Castillo-Ruiz F J, Sola-Guirado R R, Gil-Ribes J A. An automatic trunk-detection system for intensive olive harvesting with trunk shaker. Biosystems Engineering, 2018; 172: 92–101.

[6] Sola-Guirado R R, Aragon-Rodriguez F, Castro-Garcia S, Gil-Ribes J. The vibration behaviour of hedgerow olive trees in response to mechanical harvesting with straddle harvester. Biosystems Engineering, 2019; 184: 81–89.

[7] Dang K H, Niu Z J, Mu H T, Lan W K, Zhang X, Xin D, et al. Vibration harvesting process of olive trees based on response surface methodology and rigid-flexible coupling simulation. Int J Agric & Biol Eng, 2025; 18(3): 25–36.

[8] Zhang W Q, Li Z Z, Tan Y Z, Li W. Optimal design and experiment on variable pacing combing brush picking device for *Lycium barbarum*. Transactions of the CSAM, 2018; 49(8): 83–90. (in Chinese)

[9] Guo Y L, Bao Y D, He P Z, Wang H B. Design and experiment of hand-push lowbush blueberry picking machine. Transactions of the CSAE, 2012; 28(7): 40–45. (in Chinese)

[10] Du X Q, Ning C, He L Y, Qian Y, Zhang G F, Yao X H. Design and test of crawler-type high clearance *Camellia oleifera* fruit vibratory harvester. Transactions of the CSAM, 2022; 53(7): 113–121. (in Chinese)

[11] Homayouni T, Maharlooei M, Toudeshki A, Ferguson L, Ehsani R. Simultaneous trunk and canopy shaking improves table olive harvester efficiency versus trunk shaking alone. Horticulturae, 2023; 9(6): 640.

[12] Pu Y J, Toudeshki A, Ehsani R, Yang F Z. Design and evaluation of a two-section canopy shaker with variable frequency for mechanical harvesting of citrus. Int J Agric & Biol Eng, 2018; 11(5): 77–87.

[13] Zhuo P, Li Y, Wang B S, Jiao H B, Wang P, Li C S, Niu Q, Wang L H. Analysis and experimental study on vibration response characteristics of mechanical harvesting of jujube. Computers and Electronics in Agriculture, 2022; 203: 107446.

[14] Sola-Guirado R R, Sánchez-Cachinero P, Blanco-Roldán G. Simultaneous trunk and branch shaking in an over-the-row olive harvester. Biosystems Engineering, 2023; 231: 92–103.

[15] Rao H H, Hang D S, Wang Y L, Chen B, Liu M H. Design and experiment of hydraulic-driven Camellia fruit picking machine. Transactions of the CSAM, 2019; 50(5): 133–139, 147. (in Chinese)

[16] Malladi A, Vashisth T, NeSmith S. Development and evaluation of a portable, handheld mechanical shaker to study fruit detachment in blueberry. HortScience, 2013; 48(3): 394–397.

[17] Wu D L, Fu L Q, Cao C M, Li C, Xu Y P, Ding D. Design and experiment of shaking-branch fruit picking machine for Camellia fruit. Transactions of the CSAM, 2020; 51(11): 176–182, 195. (in Chinese)

[18] Du X Q, Ni K N, Wu C Y. Vibratory harvesting mechanism for tree fruit based on epitrochoid. Transactions of the CSAM, 2016; 47(3): 59–66. (in Chinese)

[19] Han M, Xiong B, Liu J, Yang D, Li T. Drive layout configuration strategy and scale optimization design of multi-drive mode parallel mechanism. Journal of Mechanisms and Robotics, 2024; 16(9): 091002.

[20] Lin C S, Lee T. A classification method for input joints of planar five-bar mechanisms. Mechanism and Machine Theory, 2003; 38(11): 1307–1322.

[21] Sun Y, Liu Y, Zou T, Jin M, Liu H. Design and optimization of a novel six-axis force/torque sensor for space robot. Measurement, 2015; 65: 135–148.

[22] Baron N, Philippides A, Rojas N. A novel kinematically redundant planar parallel robot manipulator with full rotatability. Journal of Mechanisms and Robotics, 2018; 11(1): 011008.

[23] Wen K, Gosselin C M. Forward kinematic analysis of kinematically redundant hybrid parallel robots. Journal of Mechanisms and Robotics, 2020; 12(6): 061008.

[24] Awad M I, Hussain I, Ghosh S, Zweiri Y, Gan D. A double-layered elbow exoskeleton interface with 3-PRR planar parallel mechanism for axis self-alignment. Journal of Mechanisms and Robotics, 2020; 13(1): 011016.

[25] Du X Q, Han X T, Shen T F, Li S T, He L Y. Design and experiment of two-degree-of-freedom canopy shaking equipment based on 5R parallel mechanism. Transactions of the CSAM, 2023; 54(4): 96–106. (in Chinese)

[26] Wang R Y, Fang D, Wu C, Wang B Y. Dynamic response of *Camellia oleifera* fruit-branch based on mathematical model and high-speed photography. Biosystems Engineering, 2024; 237: 232–241.

[27] Chen K Z. Design and research on canopy shaking harvester for *Camellia oleifera* fruit. MS thesis, Zhejiang Sci-Tech University, 2020. (in Chinese). DOI: 10.27786/d.cnki.gzjlg.2020.000650.